TABLE II
DEPENDENCE OF R_g/R_h ON SHAPE

Shape	R_g/R_h
Sphere	0.77
Oblate Ellipsoid	0.94
Rod	1.87

assembly was 0.77 μg/ml at 5°C, 2.4 μg/ml at 25°C, and 7.7 μg/ml at 37°C.

Biologic activity, as measured by ristocetin-dependent platelet agglutination using nephelometry (7), was found to depend directly on polymer size (Fig. 2), with both $\overline{R}_g$ and $\overline{R}_h$ varying similarly with activity. The ratio of the slopes of these lines is one, suggesting that the overall solution shape of vWF does not vary with changes in multimer length.

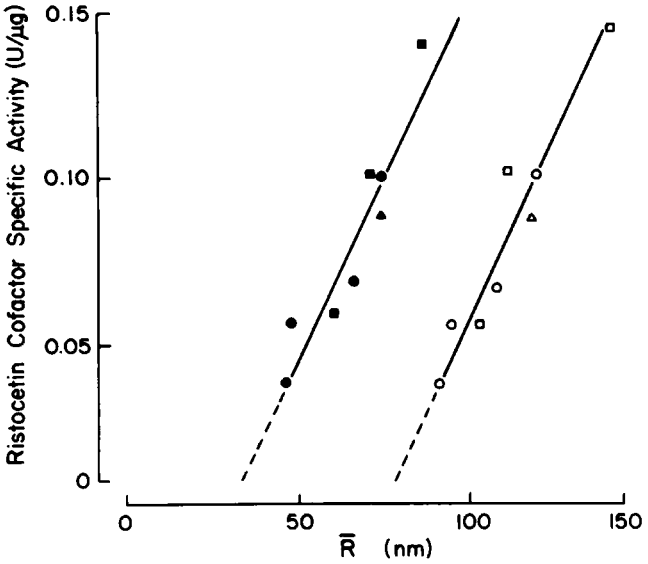

FIGURE 2 Ristocetin-dependent platelet-agglutinating activity of vWF as a function of solution radii. Fractions of three different preparations (closed symbols) of vWF obtained from Sephacryl S-1000 column chromatography (Sephadex), used to purify vWF from a cryo-precipitate of plasma and to fractionate its multimer distribution (8), were tested for biologic activity (i.e., platelet agglutination); the same fractions were analyzed by QLS. Activity (one unit defined as that found in 1 ml of normal human plasma) is plotted as a function of $\overline{R}_g$ (open symbols) and of $\overline{R}_h$ (closed symbols).

These data show that: (*a*) vWF is a flexible, linear polymer composed of repeating protomers; (*b*) the flexible, coiled configuration of the polymer noted by EM exists in solution as well; (*c*) disulfide bonds maintain polymer size at physiologic concentrations, but noncovalent forces support protomer association at higher concentrations and are possibly important for intracellular assembly; and (*d*) size and shape are directly correlated with biologic activity.

These studies were supported by National Institutes of Health grants GM14237, HL17513, HL35014, and 5T32HL07049. J. Loscalzo is the recipient of an American Heart Association Clinician-Scientist Award.

Received for publication 16 April 1985.

REFERENCES

1. Legaz, M. E., G. Schmer, R. B. Counts, and E. W. Davie. 1973. Isolation and characterization of human factor VIII. *J. Biol. Chem.* 248:3946–3955.
2. Shapiro, G. A., J. C. Anderson, S. V. Pizzo, and P. A. McKee. 1973. The subunit structure of normal and hemophilic factor VIII. *J. Clin. Invest.* 52:2198–2210.
3. Hovig, T., and H. Stormorken. 1974. Ultrastructural studies on platelet plug formation in bleeding time wounds from normal individuals and patients with von Willebrand's disease. *Acta Pathol. Microbiol. Scand.* 248:105–122. (Suppl.)
4. Van Mourik, J. A., B. N. Bouma, W. T. La Brugere, S. De Graf, and I. A. Mechtar. 1974. Factor VIII, a series of homologous oligomers and a complex of two proteins. *Thromb. Res.* 4:155–162.
5. Counts, R. B., S. L. Paskell, and S. K. Elgee. 1978. Disulfide bonds and the quaternary structure of factor VIII/von Willebrand factor. *J. Clin. Invest.* 62:702–709.
6. Loscalzo, J., M. Fisch, and R. I. Handin. 1985. The quaternary structure and assembly of human von Willebrand protein. *Biochemistry.* In press.
7. Born, G. V. R., and M. J. Cross. 1963. The aggregation of blood platelets. *J. Physiol. (Lond.).* 168:178–195.
8. Loscalzo, J., and R. I. Handin. 1984. Conformational domains and structural transitions of human von Willebrand protein. *Biochemistry.* 23:3880–3886.

QUANTITATIVE ELECTRON MICROSCOPIC ANALYSIS OF MICROCRYSTALLINE PROTEIN ARRAYS

A Few Precautionary Notes

DOUGLAS L. DORSET
Electron Diffraction Department, Medical Foundation of Buffalo, Inc., Buffalo, New York 14203

Electron microscopic studies of macromolecular microcrystals (1) have shown that, despite the 7 Å-resolution limit imposed by radiation damage for unstained materials, hope remains to use the 3 Å data (for example) found in electron diffraction patterns. While initial image studies utilize negatively stained preparations (~20 Å resolution)

BIOPHYS. J. © Biophysical Society · 0006–3495/86/01/50/04 $1.00
Volume 49 January 1986 50–53

(2) with detail extended via unstained microcrystals, several error sources are considered beside beam damage, among them specific stain interactions (3); electron microscope objective lens aberrations (4); and the missing cone of data set by goniometer tilt limits (5). Often ignored, however, are the electron scattering characteristics of the specimen itself and their role in image interpretation. Recent calculations in our laboratory (6) indicate that the often-assumed predominant role of lens aberration to image distortion (7) can be dangerous oversimplification, particularly for negatively stained samples.

Multislice *n*-beam dynamical calculations for a model three-dimensional crystal structure based on *Escherichia coli* ompF matrix porin (8), extends earlier work (9). The model unit cell consists of two 100 Å-thick layers (p3 symmetry) mutually rotated to give space group $P6_3$ (Fig. 1). For each layer, the phase grating terms

$$q(x,y) = \exp[-i\sigma\rho(x,y)\Delta z - \mu(x,y)]$$

were calculated (20 successive slices) for incorporation into the dynamical calculation (9). Here $\rho(x,y)$ is the projected slice potential (Δz = 5 Å); σ is a wavelength-dependent interaction constant; and $\mu(x,y)$ is a phenomenological absorption term. Image calculations reveal alternation of p3 and p6 projections until, beyond 500 Å, there is a breakdown of projected image symmetry (Fig. 1). Thus, the direct interpretation of 20 Å-resolution, 100 kV electron images from >1,000 Å-thick negatively stained crystals (2), in fact, yields erroneous structure. Use of data from two-dimensional reconstituted membrane protein crystals ≤ 100 Å thick, on the other hand, is quite reasonable.

Resolution extension to the 3 Å (for example) found in electron diffraction patterns could be frustrated by the observed presence of crystal bending (10, 11). Projection down a long unit cell axis causes an effective loss of diffraction coherence due to the bend-induced attenuation of long Patterson vectors (11), according to the expression for observed diffraction intensity $I_{hk\ell}$, expressed as the Fourier transform of the Patterson function,

$$I_{hk\ell} = \sum_i W_i \exp(2\pi r_i \cdot s_{hk\ell}) \exp(-\pi^2 c^2 s_{hk\ell}^2 z_i^2),$$

where W_i is the form factor of Patterson peak i at position r_i. The Gaussian function, based on crystal bending c, the reciprocal vector $s_{hk\ell}$, and the z_i component of the Patterson vector i, attenuates the intensity, such that the contribution of a particular Patterson peak is zero if $z_i > z_0 = (c\pi s)^{-1}$.

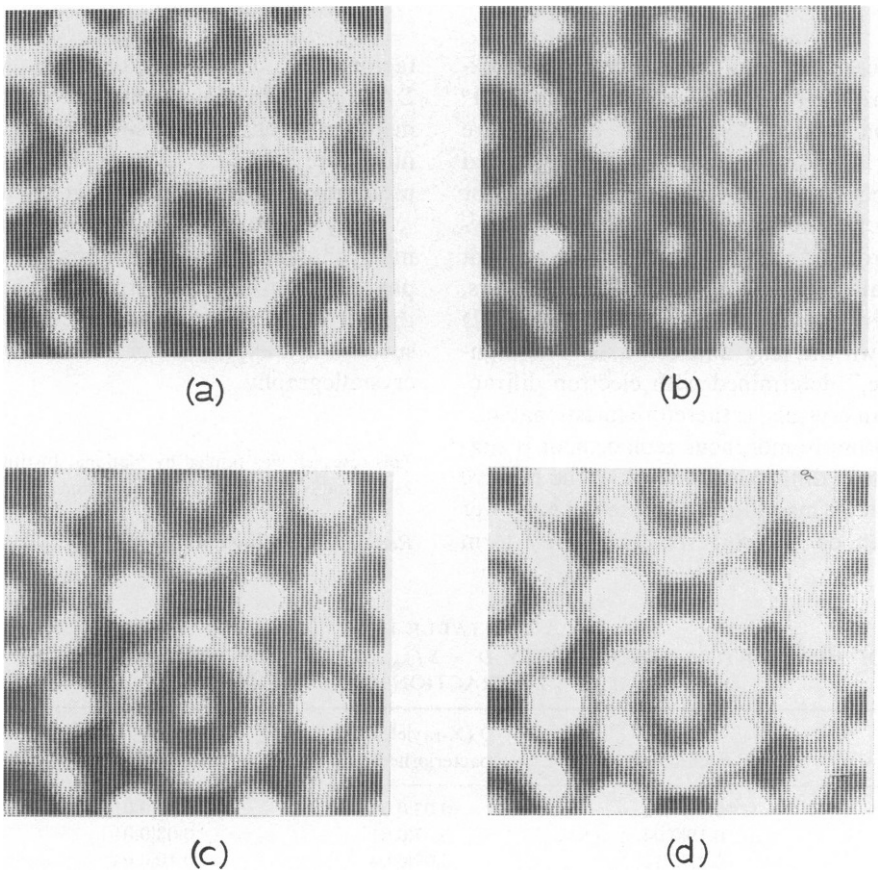

FIGURE 1 *N*-beam dynamical images of a UAc negatively stained protein crystal at 20 Å resolution: (*a*) t = 100 Å, one layer; (*b*) t = 200 Å, one unit cell of two layers; (*c*) t = 600 Å, note slight deviation from p6 symmetry; (*d*) t = 1000 Å, note changes in image density. (See reference 6 for further description.)

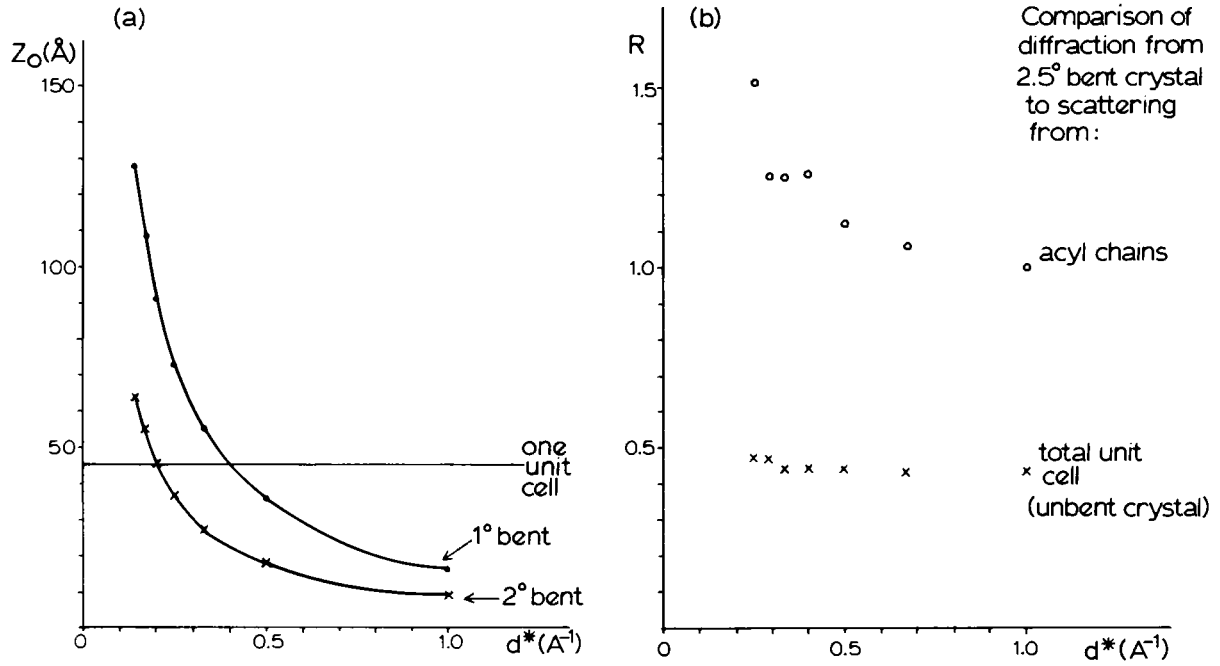

FIGURE 2 Effect of bending on the electron diffraction intensity from a thin crystal: (*a*) Evaluation of $z_0 = (\pi cs)^{-1}$ vs. data resolution for two bend values. Note that the scattering coherence for large structures becomes less than the projected unit cell length, e.g., t = 45 Å. (*b*) Diffraction intensity calculation for bend distorted cholesteryl myristate monolamellae ($t \simeq$ 50 Å) vs. data resolution. A comparison of a 2.5° bent structure with the unbent structure shows that no simple interpretation of the data can be made.

The apparent coherent scattering is <100 Å layer thickness beyond 5.5 Å resolution if the crystal is bent by 1° (Fig. 2), a situation further complicated by structure dependence. Model calculations for solution-crystallized phospholipids (projected lamellar spacing of 48 Å), for example, reveal only features of the fatty acid polymethylene subcell in electron diffraction patterns, in agreement with actual structural analysis (12). For cholesteryl esters, one cannot even determine the acyl chain packing (Fig. 2) in the projection down the long unit cell axis. The high-resolution "structure," determined with electron diffraction from bent protein crystals, is therefore questionable.

Although heavy atom isomorphous replacement is suggested to phase electron diffraction data (13), the relative electron scattering factor magnitudes represent a narrower range of values than do the corresponding x-ray form factors (14). Given the detectibility, $D = \Sigma f^2_{\text{heavy atom}}/\Sigma f^2_{\text{light atom}}$, the phase contribution from the heavy atom inclusion is considerably smaller for electron diffraction, as illustrated in Table I. Thus, it will be difficult to obtain useful phase information with conventional stains.

Every structural probe has its limitations. Assuming too much analogy of electron microscopy to x-ray crystallography can lead to flawed structure determinations. Within the permitted boundaries, however, the technique can be successfully exploited for all its advantages over x-ray crystallography.

This research was funded by National Institutes of Health grant GM-21047 and National Science Foundation grant INT82-13903.

Received for publication 8 April 1985.

TABLE I
COMPARISON OF HEAVY ATOM DETECTIBILITY $D = \Sigma f^2_{\text{heavy}}/\Sigma f^2_{\text{light}}$ IN PROTEIN MOLECULES VIA X-RAY AND ELECTRON DIFFRACTION MEASUREMENTS

Heavy atom	Cytochrome b5	D (X-ray|electron) bacteriorhodopsin	α-amylase*	catalase*
I	0.08|0.03	0.03|0.01	0.03|0.01	0.01|0.006
Hg	0.19|0.04	0.07|0.01	0.08|0.01	0.03|0.006
U	0.25|0.11	0.09|0.04	0.10|0.04	0.04|0.02
MW	9755	26,000	96,000	250,000

*Tetrameric—one heavy atom assumed/monomer.

REFERENCES

1. Unwin, P. N. T., and R. Henderson. 1975. Molecular structure determination by electron microscopy of unstained crystalline specimens. *J. Mol. Biol.* 94:425–440.
2. Vainshtein, B. K. 1978. Electron microscopical analysis of the three-dimensional structure of biological macromolecules. *Adv. Opt. Electron Microsc.* 7:281–377.
3. Steven, A. C., and M. A. Navia. 1982. Specificity of stain distribution in electron micrographs of protein molecules contrasted with uranyl acetate. *J. Microsc.* 128:145–155.
4. Erickson, H. P. 1973. The Fourier transform of an electron micrograph-first order and second order theory of image formation. *Adv. Opt. Electron Microsc.* 5:163–199.
5. Engel, A., and A. Massalski. 1984. 3D reconstruction from electron micrographs: Its potential and practical limitations. *Ultramicroscopy.* 13:71–84.
6. Dorset, D. L., 1984. Dynamical electron scattering from negatively stained protein microcrystals. *Ultramicroscopy.* 13:311–324.
7. Klug, A. 1978-1979. Image analysis and reconstruction in the electron microscopy of biological macromolecules. *Chem. Scripta.* 14:245–256.
8. Dorset, D. L., A. Engel, A. Massalski, and J. P. Rosenbusch. 1984. Three-dimensional structure of a membrane pore. Electron microscopical analysis of *Escherichia coli* outer membrane matrix porin. *Biophys. J.* 45:128–129.
9. Grinton, G. R., and J. M. Cowley. 1971. Phase and amplitude contrast in electron micrographs of biological material. *Optik.* 34:221–233.
10. Baldwin, J., and R. Henderson. 1984. Measurement and evaluation of electron diffraction patterns from two-dimensional crystals. *Ultramicroscopy.* 14:319–336.
11. Cowley, J. M. 1961. Diffraction intensities from bent crystals. *Acta Crystallogr.* 14:920–927.
12. Dorset, D. L. 1983. Electron crystallography of alkyl chain lipids; identification of long chain packing. *Ultramicroscopy.* 12:19–28.
13. Dumont, M. E., J. W. Wiggins, and S. B. Hayward. 1980. Electron diffraction of platinum labeled bacteriorhodopsin. Proc. Electron Microsc. Soc. America, 38th Annual Meeting, San Francisco, CA. Claitor's Press, Baton Rouge. 34–35.
14. Doyle, P. A., and P. S. Turner. 1968. Relativistic Hartree-Fock x-ray and electron scattering factors. *Acta Crystallogr.* A24:390–397.

HYDRATED MACROMOLECULAR ASSEMBLY STRUCTURE REVEALED BY FREEZE-ETCH STEREO-ELECTRON MICROSCOPY

Spermidine-DNA Toruses and RNA Polymerase-DNA Complexes

KENNETH A. MARX AND GEORGE C. RUBEN

Departments of Chemistry and Biology, Dartmouth College, Hanover, New Hampshire 03755

Hydrated macromolecules can be visualized using the freeze-fracture, deep-etch (FET) protocol. By fracturing, etching the specimen at -100°C, then cooling it to -174°C in a 5×10^{-8} torr vacuum, a 7–10 Å surface coating of Pt-C (45°) can resolve 10–20 Å specimen surface details by using transmission electron microscopy (TEM). In contrast to uncoated molecules, which begin disintegrating during the first micrograph, 10 or more micrographs in a tilt series of a single Pt-C coated molecule can be recorded with a eucentric goniometer without specimen replica deterioration. Using pairs of stereomicrographs of magnification M, separated by the tilt angle θ, parallax measurements of height H can reveal three-dimensionsal topography of macromolecular complexes using the parallax equation

$$H = (P_H - P_L)/2M \sin(\theta/2). \quad (1)$$

This methodology has advantages over other preparative and physical techniques. The FET visualizes hydrated specimens, whereas other EM techniques require a dehydrated specimen or embedding in the high salt and unusual pH of negative stains. Unlike x-ray or neutron diffraction and NMR spectroscopy, which look at ordered or freely diffusing molecular populations in large mass quantities, in FET individual molecules are imaged in submicrogram quantities in a noncrystalline sample. Furthermore, the FET may be applied to any kind of macromolecular assembly, and stereoscopic height measurements from the object replica have been shown to achieve a 95% fractile precision in the 5–10 Å range (1). Stereoscopic imaging complements structural data obtained by x-ray and neutron diffraction, light scattering and, to a much lesser extent, NMR spectroscopy. In contrast to light and neutron scattering, FET can measure the dimensions and topographic features of individual objects in a series of tilt views rather than fitting an averaged scattering intensity to a generalized model scattering object. This advantage is illustrated by the two systems presented here: the spermidine-condensed DNA toruses, which are in vitro model systems for DNA packing in bacteriophage and certain viruses, and the RNA polymerase-DNA ternary complex.